Changes in the Submandibular Salivary Gland Epithelial Cell Subpopulations During Progression of Sjögren's Syndrome-Like Disease in the NOD/ShiLtJ Mouse Model

ELISE M. GERVAIS[1,2], **KARA A. DESANTIS**[1,2], **NICHOLAS PAGENDARM**[1], **DEIRDRE A. NELSON**[1], **TONE ENGER**[3], **KATHRINE SKARSTEIN**[4], **JANICKE LIAAEN JENSEN**[3], and **MELINDA LARSEN**[1,*]

[1]Department of Biological Sciences, State University of New York, University at Albany, Albany, New York

[2]Molecular, Cellular, Developmental, and Neural Biology Graduate Program, State University of New York, University at Albany, Albany, New York

[3]Department of Oral Surgery and Oral Medicine, Faculty of Dentistry, University of Oslo, Oslo, Norway

[4]Department of Clinical Medicine, Section for Pathology, University of Bergen, Bergen, Norway

Abstract

Sjögren's syndrome (SS), an autoimmune exocrinopathy, is associated with dysfunction of the secretory salivary gland epithelium, leading to xerostomia. The etiology of SS disease progression is poorly understood as it is typically not diagnosed until late stage. Since mouse models allow the study of disease progression, we investigated the NOD/ShiLtJ mouse to explore temporal changes to the salivary epithelium. In the NOD/ShiLtJ model, SS presents secondary to autoimmune diabetes, and SS disease is reportedly fully established by 20 weeks. We compared epithelial morphology in the submandibular salivary glands (SMG) of NOD/ShiLtJ mice with SMGs from the parental strain at 12, 18, and 22 weeks of age and used immunofluorescence to detect epithelial proteins, including the acinar marker, aquaporin 5, ductal cell marker, cytokeratin 7, myoepithelial cell marker, smooth muscle α-actin, and the basal cell marker, cytokeratin 5, while confirming immune infiltrates with CD45R. We also compared these proteins in the labial salivary glands of human SS patients with control tissues. In the NOD/ShiLtJ SMG, regions of lymphocytic infiltrates were not associated with widespread epithelial tissue degradation; however, there was a decrease in the area of the gland occupied by secretory epithelial cells in favor of ductal epithelial cells. We observed an expansion of cells expressing cytokeratin 5 within the ducts and within the smooth muscle α-actin$^+$ basal myoepithelial population. The altered acinar/ductal ratio within the NOD/ShiLtJ SMG likely contributes to salivary hypofunction, while the expansion of cytokeratin 5 positive-basal cells may reflect loss of function or indicate a regenerative response.

---

*Correspondence to: Melinda Larsen, Department of Biological Sciences, Life Sciences 1086, State University of New York, University at Albany, 1400 Washington Avenue, Albany, NY 12222. ; Email: mlarsen@albany.edu
Elise M. Gervais and Kara A. DeSantis contributed equally to this work.

INTRODUCTION

Sjögren's syndrome (SS) is an autoimmune exocrinopathy that affects the salivary glands, lacrimal glands, and in some cases other excretory organs. Millions of Americans have been diagnosed with SS and many remain undiagnosed, with estimates ranging from 0.05% to 4.8% of the population being affected (Mavragani and Moutsopoulos, 2010; Goransson et al., 2011). The majority of SS patients are women over the age of 40 (9:1 female to male patient ratio), although SS has been diagnosed in men, younger women, and even children (comprehensively reviewed by Tincani et al., 2013). The clinical manifestations of SS include dry mouth, dry eye, and other xeroses together with neuropathies (reviewed by Fox, 2007). Classification criteria for SS were standardized in 2002 with the American-European Consensus Group criteria (Vitali et al., 2002). These criteria include experiencing at least 3 months of dry eye and dry mouth symptoms, confirmation with flow rate tests, positive tests for autoantibodies characteristic of SS, as well as a salivary gland biopsy that is positive for focal lymphocytic infiltrates; four out of six tests have to be positive for the patient to be classified as having SS and the presence of autoantibodies or a positive biopsy is mandatory. A revision of the classification criteria used for SS was proposed in 2012 by the American College of Rheumatology (ACR) (Shiboski et al., 2012). The newly proposed ACR criteria require the presence of two out of three of the following tests; an ocular surface damage test, a blood test positive for SS autoantibodies, and a salivary gland biopsy positive for lymphocytic infiltrates (Shiboski et al., 2012). The diagnosis of SS is frequently (in about 60% of patients), complicated by symptoms of another autoimmune disease such as rheumatoid arthritis, or systemic lupus erythematosus (reviewed by Tincani et al., 2013) and this is classified as secondary SS. Patients diagnosed with SS without complications from another autoimmune disease are classified as primary SS patients. Several factors thought to contribute to SS disease onset and progression have been identified, including genetic abnormalities, exposure to viral infection, as well as hormonal changes (reviewed by García-Carrasco et al., 2006 and Tzioufas et al., 2012). However, the triggers for SS may be multifactorial and differ between patients, and no single event is known to be responsible for the decreased salivary function.

SS manifests as a progressive loss in saliva secretion that often goes undetected until saliva flow has been significantly reduced. In healthy salivary glands, secretory acinar cells make up spherical secretory units surrounding a hollow central lumen (reviewed by Holmberg and Hoffman, 2014 and Tucker, 2007). Secretion of salivary products involves vesicle release coupled with water flow into a central lumen that is continuous with the ductal network of the gland. The ductal cells modify the saliva as it is transported to the oral cavity. Previous studies have indicated that there is an increase in the ductal cell population accompanying a loss of acinar cells in SS (Daniels, 1984), although subsequent studies have revealed considerable heterogeneity in the extent of acinar loss and ductal dysplasia in these patients (Dawson et al., 2000; Beroukas et al., 2001; Goicovich et al., 2003). Myoepithelial cells

surrounding the acini and some of the ducts promote salivary gland structure by producing basement membrane and regulatory growth factors, and facilitating the secretion of saliva by contraction (Redman, 1994; Ianez et al., 2010; Kandagal et al., 2013; Tamgadge et al., 2013), and a decrease in the myoepithelial cell population has been reported in the parotid glands of some SS patients (Nashida et al., 2013). As patients are typically diagnosed late in disease and display considerable heterogeneity in tissue atrophy, cellular mechanisms contributing to disease progression are not well understood.

Several mouse models for SS have been used to study SS disease progression (Lavoie et al., 2011), including the non-obese diabetic ShiLtJ (NOD/ShiLtJ) mouse (Makino et al., 1980; Humphreys-Beher et al., 1994). The NOD/ShiLtJ mice develop autoimmune diabetes around 4 weeks of age and an autoimmune exocrinopathy that shows significant similarities to SS becomes evident between 8 and 12 weeks (Karnell et al., 2014). Decreasing saliva secretion with SS disease progression in the NOD/ShiLtJ mouse has been previously documented to be similar to human SS disease progression (Lodde et al., 2006; Soyfoo et al., 2007). As SS progresses in the NOD/ShiLtJ mouse, multiple autoantibodies develop, including characteristic anti-Ro and anti-La autoantibodies (Lavoie et al., 2010; Donate et al., 2014; Karnell et al., 2014). The SS phenotype is known to occur earlier in the submandibular salivary gland (SMG) of female mice than in other salivary glands or lacrimal glands, and the SS phenotype is seen significantly earlier in female SMGs than in male SMGs (Jayasinghe et al., 1990; Perez-Moreno et al., 2003; Xuan et al., 2013). Although the disease progression of both diabetes and SS phenotypes has been characterized in the NOD/ShiLtJ mouse (Nashida et al., 2013), changes in the salivary epithelial cell populations have not been thoroughly examined.

The goal of this study was to evaluate changes in the submandibular salivary gland epithelial cell subpopulations during progression of SS-like disease in the NOD/ShiLtJ mouse model. We compared the structure and organization of the SMG epithelium from female NOD/ShiLtJ mice at 12, 18, and 22 weeks of age to sex- and age-matched parental strain control (CD-1) SMGs. These time points were examined in order to investigate changes in the SMG epithelium during early, mid, and late stage disease in female mice. We confirmed disease progression in the NOD/ShiLtJ animals by identifying and measuring the size of focal lymphocytic infiltrates within the SMG. We examined Aquaporin 5 (Aqp5) as a marker of secretory acinar epithelium, cytokeratin 7 (K7) as a marker of the ductal epithelium, and smooth muscle α-actin (SM α-actin) as a marker of the myoepithelial population. We also looked at cytokeratin 5 (K5), which is a reported basal epithelial cell and progenitor cell marker in salivary glands and other branched organs (Vitale-Cross et al., 2004; Knox et al., 2010; Rios et al., 2014; Zuo et al., 2014). To evaluate potential for human disease relevance, we also interrogated these epithelial cell markers in human SS and non-SS patient samples and in autopsy samples derived from labial salivary gland biopsies.

MATERIALS AND METHODS

Mouse Tissue Samples

Nonobese diabetic (NOD) ShiLtJ female mice (Jackson Laboratories Labs, Bar Harbor, ME) and control female CD-1 mice (Charles River, Wilmington, MA) were received by the

University at Albany animal facility at 7 weeks of age. Due to previous reports of stress affecting the autoimmune phenotype (Cha et al., 2002; Lodde et al., 2006), both the NOD/ShiLtJ and CD-1 mice were housed under sterile conditions, kept on a 12 h/12 h light/dark cycle, and the room was entered only once per day by facility staff. Although mice were initially fed sterile (autoclaved) chow (20% fat) and water *ad libitum*, NOD/ShiLtJ mice were switched to dampened chow at approximately 18 weeks of age due to a wasting phenotype in a small subset of mice. This phenotype may have been due to significantly decreased saliva flow shown previously in this mouse model (Jonsson et al., 2006), but we cannot confirm this as a cause. However, following the transition to wet chow, all of the NOD/ShiLtJ mice showed increased activity and improved fur coat quality, indicative of improved general health.

At 8, 12, 18, or 22 weeks of age, mice were euthanized following the University at Albany IACUC-approved procedures, as previously described (Daley et al., 2009, 2011), and submandibular salivary glands were removed from each mouse. We collected tissues from a total of six mice per time point for each mouse strain. Tissues were chopped into small pieces immediately following harvest, incubated overnight in 10% Neutral Buffered Formalin (Sigma Aldrich, St. Louis, MO), and then moved to 70% ethanol for storage until paraffin embedding by Histoserv Inc. (Germantown, MD).

Human Tissue Samples

Human tissue samples were obtained from patients that were seen at the University of Oslo or at the Oslo University Hospital, Rikshospitalet, Oslo, Norway. All tissue acquisition was performed according to protocols and procedures approved by the Norwegian Committee for Ethics in Research. Labial gland biopsies were processed at the University of Oslo diagnostic pathology labs by fixation in 4% formalin, followed by embedding in paraffin to generate formalin-fixed, paraffin-embedded (FFPE) samples. The FFPE tissue specimens were transferred to a research biobank at University of Oslo. Cadaver tissue was obtained from donors without SS or other rheumatic disease from Oslo University Hospital, Ullevål, The Intrinsic Institute, and transferred to the biobank. All patient records were prepared and maintained at the University of Oslo biobank, and samples were de-identified before being sent to the Larsen Laboratory. Paraffin blocks were obtained containing labial salivary glands from seven autopsy tissue donors (five males, two females, ages ranging from 58 to 73 at time of death, average =65), eight patients diagnosed with SS (SS, all female patients, ranging in age from 48 to 84, average =60), and from six patients presenting with a combination of three or more SS symptoms but lacking autoantibodies and having focus scores below 1, therefore not meeting the 2002 American-European Consensus Group criteria (Vitali et al., 2002) for SS (non-SS, all female patients, ranging in age from 42 to 61, average =52). All biopsies were reexamined by one oral pathologist.

Tissue Microarray Construction, Selection, Preparation, and Imaging

Tissue microarrays (TMAs) were constructed from both human and mouse tissue samples. The mouse tissue TMAs were constructed to accommodate 12 CD-1 and 12 NOD/ShiLtJ SMG tissue cores for each time point, representing duplicate samples per mouse. Three CD-1 embryonic day 16 tissues, two postnatal day 1 SMG tissues, and two postnatal day 5

SMG tissues were used as positive controls for IF. The human TMA contained 15 labial salivary gland autopsy tissue spots, eight non-SS tissues spots, and 16 SS tissue spots, with one to three cores used from each patient. Four adult CD-1 mouse SMG tissue spots were also included in the human tissue TMA as positive control tissues for immunofluorescence (IF).

The TMAs were designed so tissue types were randomized and asymmetrically placed to aid in section orientation. Tissue cores (1.5 mm diameter) were removed from each FFPE block and placed into an acceptor block (containing prepunched 1.5 mm holes) to generate the TMA, (as previously described Gerdes et al., 2013; Nelson et al., 2013) by Pantomics (Richmond, CA). Five micron sections were cut from the TMA and were selected for use in this study based on the criteria that all tissues were present, there was no damage to the wax near the tissues, and none of the tissue samples were curling or rolling at the edges.

TMA slides were deparaffinized and subjected to antigen retrieval, blocking, and multiplexed immunofluorescence, using MultiOmyx methods, as previously described (Gerdes et al., 2013; Nelson et al., 2013). Images were collected from each of 104 spots on each mouse TMA slide and 44 spots on each human TMA slide using a fully automated Olympus IX-81 microscope with a 20× Plan Apo 0.75 NA objective using software developed by GE Global Research, as previously described (Gerdes et al., 2013; Nelson et al., 2013). After DAPI staining but before processing samples for IF, background images were captured for each channel. After each round of IF chemical inactivation, slides were imaged to verify loss of signal from the prior antibody round and were subjected to additional chemical inactivation steps, as required.

Multiplexed Immunofluorescence and Imaging

Both human and mouse TMA slides were subjected to multiplexed immunofluorescence with antibodies to detect epithelial cadherin (ECAD) (BD Biosciences, 610182), smooth muscle α-actin (SM α-actin) (Sigma, C6198), cytokeratin 7 (K7) (Abcam, Cambridge MA, ab9021), cytokeratin 5 (K5) (Covance, Princeton NJ, PRB160P), CD4 (Novus Biologicals, Littleton CO, NBP1-19371, Human Only), CD45R (Millipore, Billerica MA, 557683, Mouse Only), aquaporin 5 (Aqp5) (Alomone, aqp-005), Na^+/K^+-ATPase (Epitomics 2047-1), and nuclei were stained using DAPI (Life Technologies, Carlsbad CA, D1306). Antibodies were applied either as a primary antibody and detected with a secondary antibody (Affini-Pure F (ab′) 2 fragments) conjugated either to Cy3 or Cy5 (Jackson ImmunoResearch, West Grove, PA) or as an antibody directly conjugated to either Cy3 or Cy5. The second antibody and all subsequent antibodies applied of a given species were applied as a direct conjugate. The Cy3 and Cy5 fluorescence was chemically inactivated and the slides were washed before the application of each subsequent round of antibodies.

Virtual Hemotoxylin and Eosin (H&E) Images

DAPI and background images were processed by GE Global Research (Niskayuna, NY) to construct virtual H&E images (VH&E). Nuclei were pseudo colored purple and non-nuclear tissues pseudo colored pink to create a hematoxylin (H) and eosin (E)-like image, as previously described (Gerdes et al., 2013; Nelson et al., 2013).

Image Processing and Quantification

Focal infiltrate measurements were performed using the distance measurement tool in Photoshop CS6 using calibrated images. Graphs were constructed using the average foci diameter for each mouse in Prism (GraphPad).

Immunofluorescence images were processed for pixel quantification using freeware ImageJ (version 1.47) to quantify the number of pixels present in each image. Images were manually examined to ensure the tissue sample remained intact and was in focus before image processing and quantification. For the mouse TMA, samples were excluded from quantitative analysis if less than 50% of the imaged area included SMG tissue. Background subtraction was performed on each image to be used before quantification with rolling ball background subtraction with a value of 50 pixels. In order to quantify only epithelial areas within the NOD tissues, a blinded counter identified five square regions of interest (ROI) measuring 225×225 pixels within ECAD-stained areas of each tissue sample using the fixed ROI selection function in ImageJ. The total number of pixels for each stain of interest within each ROI (five per image) was imported into Microsoft Excel. Total pixel counts per ROI were averaged per image (five ROIs per image), and then averaged per mouse (two to six spots per mouse). Results were graphed together with a calculated standard error of the mean (SEM) based on the number of mice included in the group. Statistical analyses were completed using freeware (VassarStats) to perform a two-tailed Student's *t* test using the average pixel counts from images from individual mice. Images of human tissues could not be quantitatively analyzed due to the small number of heterogeneous tissue samples.

Red and green channel overlaid images were processed for quantification using freeware ImageJ 2 (FIJI version 1.49J10) (Schindelin et al., 2012) to quantify the number of red, green, and yellow pixels present in each image overlay. Images were registered using the FIJI registration function called "linear stack alignment with SIFT." Background subtraction was performed on individual raw images before quantification using the "background subtraction" function with a value of 10 pixels, followed by manual thresholding to match the original image. Three color overlay images were made using the "color merge" function. Image quantification was completed in ROIs (selected as previously described, using the "fixed region of interest selection" function) sequentially using the "Color Image 3D" histogram function. The total number of pixels within each ROI was imported into Microsoft Excel. Total pixel counts per ROI (five per image) were averaged, and then averaged per mouse (two to six spots per mouse). Results were graphed together with a calculated standard error of the mean (SEM) (GraphPad). Statistical analysis was completed using VassarStats where a two-tailed Student's *t* test was performed using the averages of the individual mice. Images of human tissues were not quantitatively analyzed due to the small number of heterogeneous samples.

Epithelial area quantification was performed using ImageJ 2, FIJI. To quantify only epithelial areas within the NOD tissues, a blinded counter identified five square regions of interest (ROI), in ECAD+ areas, as described above. Within each ROI, ducts positive for K7 and acini positive for Aqp5 were manually encircled using the "freehand selection tool." For each ROI, positively staining areas (μm^2) were measured for each marker and the values were exported into Microsoft Excel. Ductal areas positive for K7 and acinar areas positive

for Aqp5 were summed separately per ROI, representing the total epithelial area positive for each marker. Summed ROI area values were averaged per image (five ROIs per image), and then averaged per mouse (two to six spots per mouse).

Image Processing for Qualitative Comparison

Black and white images captured using an IX-81 Olympus microscope were adjusted using Adobe Photo-shop CS6 (version 13.01x64). Each set of images was optimized independently for presentation by adjusting the levels. Images were resized to 600 dpi, 0.75 inch square images before assembly into composite figures in Photoshop. Multiple channel overlaid images were constructed by linking the stained image to the DAPI image acquired at the same time, manually registering the DAPI images, eliminating the black pixels from each image, and pseudocoloring each channel in the overlay.

RESULTS

Immune Focal Infiltrates are not Accompanied by Gross Structural Changes in the NOD/ShiLtJ Epithelium

To compare structural differences between the NOD/ShiLtJ and CD-1 mouse submandibular salivary glands (SMG), we compared virtual hematoxylin and eosin (VH&E) images, prepared from representative samples derived from glands of six of each strain of mice at 8, 12, 18, and 22 weeks of age. In the NOD/ShiLtJ SMG samples (Fig. 1), large accumulations of densely packed nuclei were clearly discernible in diseased tissues but were not found in the CD-1 samples. We also prepared VH&E images from human labial salivary glands derived from SS, non-SS and autopsies. Similar nuclear accumulations were present in the SS labial glands but were absent in human autopsy tissues with small aggregates of densely packed nuclei also present in the non-SS patient samples (Fig. 2). Using immunofluorescence (IF) for both the mouse and human tissues, we confirmed that the areas of densely packed nuclei were E-cadherin (ECAD) negative (Figs. 3 and 4). Nuclear accumulations within the NOD/ShiLtJ tissues were positive for CD45R, a cell surface protein found on most B cells and some T cells (Fig. 3A). CD45R$^+$ lymphocytic infiltrates were identified in the NOD/ShiLtJ tissues as early as 12 weeks, while no CD45R$^+$ cells were identified in the CD-1 control samples at any age. No CD45R$^+$ infiltrates were found in the 8-week NOD/ShiLtJ tissues (data not shown). To quantify the lymphocytic focal infiltrates in the NOD/ShiLtJ tissues, infiltrates were measured at their widest point using the nuclear stain and CD45R localization pattern. In the NOD/ShiLtJ tissue samples, lymphocytic infiltration size shows a significant increase with disease progression between 12 and 18 weeks and a nonsignificant increasing trend between 18-and 22-week-old samples (Fig. 3B). Examination of the parenchymal tissues both proximal and distal to the lymphocytic infiltrations revealed that the epithelium in the NOD/ShiLtJ SMG tissues was very similar to the control SMG tissues at all ages, with no disruptions in overall tissue structure, according to VH&E (Fig. 1) and ECAD (Fig. 3) images. To confirm lymphocytic infiltrations in the human tissues, we used an antibody to detect CD4, a T-helper cell marker (Fig. 4A). The large accumulations of nuclei in the SS tissues as well as some accumulations within the non-SS samples were CD4$^+$, and a few CD4$^+$ cells were found scattered throughout the autopsy labial salivary gland samples. The infiltration size measurements from the SS tissue

samples showed a significantly larger focal infiltrate size as compared with the non-SS tissues (Fig. 4B). No focal infiltrates were detected in any of the human autopsy tissues samples (data not shown). These data confirm disease progression in the NOD/ShiLtJ mice, demonstrate that the infiltrates are less heterogeneous in this mouse model than in SS patients, and demonstrate there is no widespread disruption of epithelial tissue structure up to 22 weeks of age in the NOD/ShiLtJ mouse model. To investigate changes within specific epithelial cell sub-populations, we examined several markers for specific epithelial cell types with in the salivary gland.

The NOD/ShiLtJ Epithelium Exhibits a Decrease in Ratio of Acinar to Ductal Tissue

Currently, there is disagreement as to whether there are changes in the distribution of the Aqp5^{+} secretory acinar cell population in SS and in SS mouse models [Beroukas et al., 2001; Steinfeld et al., 2001; Konttinen et al., 2005; Soyfoo et al., 2007; Wang et al., 2009]. Aquaporin 5 (Aqp5) is a water channel protein found at the apical surface of polarized secretory acinar cells within the salivary gland epithelium [Ma et al., 1999; Gresz et al., 2001; Larsen et al., 2011; Nelson et al., 2013]. We observed that Aqp5 is expressed throughout the secretory acinar epithelium in both the NOD/ShiLtJ and control SMG (Fig. 5A). To quantify levels of Aqp5, we randomly selected epithelial ROIs and quantified the total number of Aqp5^{+} pixels within these areas. We observed a slight decreasing trend in the levels of Aqp5 in the NOD/ShiLtJ samples at both 18 and 22 weeks of age when compared with CD-1 age-matched controls (Fig. 5B). We also performed immunofluorescence to detect Aqp5 in human labial gland biopsy samples (Fig. 6). We found heterogeneous expression of Aqp5 within all groups of human tissues but no significant quantitative differences between SS, non-SS, and autopsy samples (data not shown).

To investigate changes to the ductal epithelium within the SMG of NOD/ShiLtJ mice, we used antibodies specific for cytokeratin 7 (K7). Cytokeratin 7 is an intermediate filament protein that is expressed by the apical cells of the stratified ductal epithelium which has been used previously as a ductal marker in the SMG [Knosp et al., 2012; Nelson et al., 2013]. We observed that K7 is expressed by ductal cells throughout the epithelium in both the NOD/ShiLtJ tissue and control tissues (Fig. 5A). Although focal infiltrates were frequently periductal, the structure and cellular localization of the K7 staining seemed unaffected by the proximity to the foci. In the NOD/ShiLtJ tissues, however, increased K7 staining was observed at both 18 and 22 weeks as compared with age-matched CD-1 control SMGs. No differences were detected at 12 weeks (data not shown). To quantify levels of K7 we randomly selected epithelial ROIs and quantified the total number of K7[+] pixels within these areas, where we detected increased levels of K7 staining in the NOD/ShiLtJ tissues as compared with the CD-1 controls (Fig. 5C). We also performed IF to detect K7 in human tissue samples and observed no obvious changes in K7 localization patterns correlating with SS (Fig. 6). We also did not observe any quantifiable changes in K7 staining in the human SS tissues relative to non-SS and autopsy tissue samples (data not shown).

Given the significant increase in levels of K7 and the decreasing trend in Aqp5 levels in the NOD/ShiLtJ mice at both 18 and 22 weeks, we questioned whether there was a change in

the relative ratio of acinar tissue to ductal tissue. To quantify this, we compared the surface area occupied by Aqp5^{+} acini and K7[+] ducts within ECAD[+] epithelial areas. We identified a statistically significant increase in the K7[+] surface area of SMG epithelium in the NOD/ShiLtJ mouse relative to the CD-1 control that was mirrored by a coordinate decrease in the Aqp5^{+} epithelial area (Fig. 5D). This change in the composition of epithelial area is independent of the epithelial cell population that is observed to be replaced by lymphocytic infiltrates with advancing disease progression in both the NOD/ShiLtJ mouse model and the human SS tissues. These results indicate that there is a decrease in the ratio of secretory acinar cell to ductal epithelial cell surface area in the NOD/ShiLtJ SMG relative to control SMG, which may be a contributing factor to the reported decrease in saliva production in this mouse model (Lodde et al., 2006; Soyfoo et al., 2007).

The NOD/ShiLtJ Epithelium Exhibit an Increase in K5 Expression in the Myoepithelium and Basal Ductal Cells

In both the mouse SMG and the human labial salivary gland, myoepithelial cells surround the acini and some of the ducts by extending long projections that wrap around the structures (Doggett et al., 1971; Redman, 2008; Amano et al., 2012). Myoepithelial cells were identified using an antibody to detect smooth muscle α-actin (SM α-actin) in regions of the tissue that were also positive for ECAD. In the NOD/ShiLtJ tissue samples, when compared with CD-1 control samples, the localization of SM α-actin was largely unchanged, including in the immediate vicinity of large focal infiltrates (Fig. 7A). However, when the levels of SM α-actin staining were quantified, a slight increase in overall SM α-actin staining was seen at 18 weeks and a significant increase in SM α-actin was seen at 22 weeks in the NOD/ShiLtJ, as compared with age-matched CD-1 control samples (Fig. 7B). In the human labial salivary glands we observed no obvious changes in SM α-actin[+] myoepithelial cell localization (Fig. 6B); however, quantification of levels of SM α-actin showed decreased levels in both the non-SS and SS tissues as compared with autopsy (data not shown).

Since a subset of SM α-actin^{+} myoepithelial cells also express cytokeratin 5 (K5) in mouse SMG (Nelson et al., 2013) and mammary glands (Gusterson et al., 2005), we examined whether a subset of the expanded SM α-actin[+] population may also express K5. Close comparison of the K5 and SM α-actin staining patterns within the NOD/ShiLtJ SMG and control samples revealed a seemingly higher incidence of K5 and SM α-actin co-localization in the myoepithelium of NOD/ShiLtJ than control tissues at both 18 and 22 weeks (Fig. 7A, yellow regions). To quantify SM α-actin[+]/K5[+] overlap, we examined ROIs of the epithelial regions excluding areas containing large ducts (identified using levels of ECAD staining). An increase in SM α-actin/K5 co-positive epithelial regions was identified in the 22-week NOD/ShiLtJ compared with age-matched controls (Fig. 7D). We also quantified the SM α-actin[+]/K5[−] (Fig. 7E) and SM α-actin[−]/K5[+] (Fig. 7F) populations within these ROIs in the epithelium outside of large ductal areas, where we found that SM α-actin^{+} myoepithelial cells did not always express K5, but most of the K5^{+} cells do also express SM α-actin, thus identifying them as myoepithelial cells. In some human SS patient samples SM α-actin/K5 co-positive cells were detected; however, more commonly we saw a loss of SM α-actin staining in the human diseased tissues (Fig. 6B). Interestingly, we also observed an increase in K5^{+} basal cells in the large striated ducts in cells that were not K7 positive (Fig. 7A).

Quantification of the K5 staining in the NOD/ShiLtJ showed a slight increase at 18 weeks and a statistically significant increase at 22 weeks when compared with CD-1 controls (Fig. 7C). In the human SS samples, a similar increase in K5 staining concentrated in the basal cells of the ductal epithelium was also seen (Fig. 6B), indicating that this feature of SS is recapitulated to some extent in the NOD/ShiLtJ model.

DISCUSSION

Here we report changes to subpopulations within the SMG epithelium in the NOD/ShiLtJ mouse model of SS. Upon confirming that the NOD/ShiLtJ mice have a SS-like immune infiltration we expected to find that, similar to disease progression in the human salivary glands, the epithelial architecture directly adjacent to the lymphocytic infiltrates in the NOD/ShiLtJ tissues would be disrupted, while the epithelium farthest from the foci would remain relatively intact. However, upon closer investigation we found that the tissue architecture up to 22 weeks, as determined by VH&E stains, the ECAD positive epithelial distributions and the Aqp5$^+$ acinar, K7$^+$ ductal, and SM α-actin$^+$ myoepithelial populations were not obviously disrupted, including tissue areas directly adjacent to the lymphocytic infiltrations. Our observations that epithelial architecture is not significantly disrupted in the NOD/ShiLtJ mouse up to 22 weeks of age is consistent with another recent report (Mellas et al., 2014), and suggests that the presence of the advanced lymphocytic infiltrates may not directly disrupt the epithelium at this stage of disease progression. In the human SS affected tissues, we observed that large areas of the epithelium are disrupted surrounding the focal infiltrates and show an amorphous morphology, consistent with other reports (Goicovich et al., 2003; Molina et al., 2006). This difference in epithelial architecture between the mouse model and human disease may indicate that the 22-week NOD/ShiLtJ phenotype does not truly mimic late stage human SS, and indicates that the later stages of disease progression require further investigation in this model.

Our investigation into the epithelial cell subpopulations led to the identification of several subtle changes within the epithelial compartment of the NOD/ShiLtJ SMG, many of which were mirrored in the qualitative analysis of the human patient samples. In the NOD/ShiLtJ model, we identified a statistically significant decrease in the ratio of the surface area of epithelium comprised of secretory acinar cells/ductal cells, which may contribute to deficits in saliva flow in the NOD/ShiLtJ mouse and suggest that changes in the ductal to acinar area ratios are an early event in the NOD/ShiLtJ model. The changes we observed in the ratio of epithelial area covered by Aqp5$^+$ acinar cells as compared with K7$^+$ ductal cells are consistent with previous reports of dysplastic ductal expansion in SS (Ihrler et al., 2000; Konttinen et al., 2006) and nonquantitative studies that identified preferential loss of the acinar population in favor of the ductal population in SS affected salivary glands (Daniels, 1984; Konttinen et al., 2005). We also found a novel increase in the myoepithelial SM α-actin staining in the NOD/ShiLtJ SMGs as compared with controls. In the human samples, consistently decreased SM α-actin was present in the SS tissues as well as in non-SS controls as compared with autopsy samples, consistent with previous reports in the NOD/ShiLtJ parotid gland that indicate decreased myoepithelial populations in SS (Nashida et al., 2013). Again, this may reflect that 22 weeks in the NOD/ShiLtJ model is not representative of human late-stage disease, or may indicate gland-specific differences in disease

progression since the human biopsies we queried are minor labial glands rather than submandibular glands. We also report an increase in the levels of the basal epithelial marker K5 in a subset of the myoepithelium and in the stratified ducts, consistent with previous reports of expansion of cells expressing basal cytokeratins in labial gland epithelia in SS patients (Palmer et al., 1986). This may be indicative of an aberrant differentiation state within the myoepithelium in parallel with expansion of the basal K5 and suprabasal K7 ductal cell expansion, which could lead to the dysplastic epithelium characteristic of more advanced disease in SS patients. Further, since $K5^+$ cells can function as SMG epithelial progenitors (Knox et al., 2010) and myoepithelial cells can participate in regenerating acinar structures in SMG damaged by ductal ligation (Cotroneo et al., 2008), these expanding $K5^+$ cells in the NOD/ShiLtJ model may be indicative of an intrinsic tissue renewal and/or repair mechanism that is activated in the disease state. Thus, anti-inflammatory and/or directed differentiation therapeutic strategies may facilitate an expanding $K5^+$ population to restore function to the regenerating epithelium for SS patients in the future.

Acknowledgments

LITERATURE CITED

Amano O, Mizobe K, Bando Y, Sakiyama K. Anatomy and histology of rodent and human major salivary glands-overview of the Japan Salivary Gland Society sponsored workshop. Acta Histochem Cytochem. 2012; 45:241–250. [PubMed: 23209333]

Beroukas D, Hiscock J, Jonsson R, Waterman SA, Gordon TP. Subcellular distribution of aquaporin 5 in salivary glands in primary Sjögren's syndrome. Lancet. 2001; 358:1875–1876. [PubMed: 11741631]

Cha S, Peck AB, Humphreys-Beher MG. Progress in understanding autoimmune exocrinopathy using the non-obese diabetic mouse: an update. Crit Rev Oral Biol Med. 2002; 13:4–16.

Cotroneo E, Proctor GB, Paterson KL, Carpenter GH. Early markers of regeneration following ductal ligation in rat submandibular gland. Cell Tissue Res. 2008; 332:227–235. [PubMed: 18335244]

Daley WP, Gulfo KM, Sequeira SJ, Larsen M. Identification of a mechanochemical checkpoint and negative feedback loop regulating branching morphogenesis. Dev Biol. 2009; 336:169–182. [PubMed: 19804774]

Daley WP, Kohn JM, Larsen M. A focal adhesion protein-based mechanochemical checkpoint regulates cleft progression during branching morphogenesis. Dev Dyn. 2011; 240:2069–2083. [PubMed: 22016182]

Daniels TE. Labial salivary gland biopsy in Sjögren's syndrome: assessment as a diagnostic criterion in 362 suspected cases. Arthritis Rheum. 1984; 30:571–589.

Dawson LJ, Smith PM, Moots RJ, Field EA. Sjögren's syndrome — time for a new approach. Br Soc Rheumatol. 2000:234–237.

Doggett RG, Bentinck B, Harrison GM. Structure and ultra-structure of the labial salivary glands in patients with cystic fibrosis. J Clin Pathol. 1971; 24:270–282. [PubMed: 4324770]

Donate AA, Voigt A, NQ. The value of animal models to study immunopatholgy of primary human Sjögren's syndrome symptoms. Expert Rev Clin Immunol. 2014; 10:469–481. [PubMed: 24506531]

Fox PC. Autoimmune diseases and Sjögren's syndrome: an autoimmune exocrinopathy. Ann NY Acad Sci. 2007; 1098:15–21. [PubMed: 17332090]

García-Carrasco M, Fuentes-Alexandro S, Escárcega RO Salgado G, Riebeling C, Cervera R. Pathophysiology of Sjögren's syndrome. Arch Med Res. 2006; 37:921–932. [PubMed: 17045106]

Gerdes MJ, Sevinsky CJ, Sood A, Adak S, Bello MO, Bordwell A, Can A, Corwin A, Dinn S, Filkins RJ, Hollman D, Kamath V, Kaanumalle S, Kenny K, Larsen M, Lazare M, Li Q, Lowes C, McCulloch CC, McDonough E, Montalto MC, Pang Z, Rittscher J, Santamaria-Pang A, Sarachan BD, Seel ML, Seppo A, Shaikh K, Sui Y, Zhang J, Ginty F. Highly multiplexed single-cell analysis of formalin-fixed, paraffin-embedded cancer tissue. Proc Natl Acad Sci USA. 2013; 110:11982–11987. [PubMed: 23818604]

Goicovich E, Molina C, Perez P, Aguilera S, Fernandez J, Olea N, Alliende C, Leyton C, Romo R, Leyton L, Gonzalez M-J. Enhanced degradation of proteins of the basal lamina and stroma by matrix metalloproteinases from the salivary gland of Sjögren's syndrome patients: correlation with reduced structural integrity of acini and ducts. Arthritis Rheum. 2003; 48:2573–2584. [PubMed: 13130477]

Goransson LG, Haldorsen K, Brun JG, Harboe E, Jonsson MV, Skarstein K, Time K, Omdal R. The point prevalence of clinically relevant primary Sjögren's syndrome in two Norwegian countries. Scand J Rheumatol. 2011; 40:221–224. [PubMed: 21231797]

Gresz V, Kwon TH, Hurley PT, Varga G, Zelles T, Nielsen S, Case RM, Steward MC. Identification and localization of aquaporin water channels in human salivary glands. Am J Physiol Gastrointest Liver Physiol. 2001; 281:G247–G254. [PubMed: 11408278]

Gusterson BA, Ross DT, Heath VJ, Stein T. Basal cytokeratins and their relationship to the cellular origin and functional classification of breast cancer. Breast Cancer Res. 2005; 7:143–148. [PubMed: 15987465]

Holmberg KV, Hoffman MP. Monographs in Oral Science. Vol 24: Saliva:Secretions and Functions. Anatomy, Biogenesis and Regeneration of Salivary Glands. 2014:1–13. Web: PMC.

Humphreys-Beher, MG.; HuY, NY.; Wang, P-L.; Purushotham, KR. Utilization of the non-obese diabetic (NOD) mouse as an animal model for the study of Sjögren's syndrome. In: Sullivan, DA., editor. Lacrimal gland, tear film and dry eye syndromes. New York: Plenum Press; 1994. p. 631-636.

Ianez RF, Buim ME, Coutinho-Camillo CM, Schultz R, Soares Fa, Lourenço SV. Human salivary gland morphogenesis: myoepithelial cell maturation assessed by immunohistochemical markers. Histopathology. 2010; 57:410–417. [PubMed: 20840670]

Ihrler S, Baretton GB, Menauer F, Blasenbreu-Vogt S, Lohrs U. Sjögren's syndrome and MALT lymphomas of salivary glands: A DNA-cytometric and interphase-cytogenetic study. Mod Pathol. 2000; 13:4–12. [PubMed: 10658904]

Jayasinghe NR, Cope GH, Jacob S. Morphometric studies on the development and sexual dimorphism of the submandibular gland of the mouse. J Anat. 1990; 172:115–127. [PubMed: 2272897]

Jonsson MV, Delaleu N, Brokstad KA, Berggreen E, Skarstein K. Impaired salivary gland function in NOD mice: association with changes in cytokine profile but not with histopathologic changes in the salivary gland. Arthritis Rheum. 2006; 54:2300–2305. [PubMed: 16802370]

Kandagal V, Redder C, Shetty S, Vibhute N, Ahamad S, Ingaleshwar P. Myoepithelial cells: current perspectives in salivary gland tumors. Clin Cancer Investig J. 2013; 2:101.

Karnell JL, Mahmoud TI, Herbst R, Ettinger R. Discerning the kinetics of autoimmune manifestations in a model of Sjögren's syndrome. Mol Immunol. 2014; 62:277–282. [PubMed: 24907930]

Knosp WM, Knox SM, Hoffman MP. Salivary gland organogenesis. Wiley Interdiscip Rev Dev Biol. 2012; 1:69–82. [PubMed: 23801668]

Knox SM, Lombaert IMa, Reed X, Vitale-Cross L, Gutkind JS, Hoffman MP. Parasympathetic innervation maintains epithelial progenitor cells during salivary organogenesis. Science. 2010; 329:1645–1647. [PubMed: 20929848]

Konttinen YT, Porola P, Konttinen L, Laine M, Poduval P. Immunohistopathology of Sjögren's syndrome. Autoimmun Rev. 2006; 6:16–20. [PubMed: 17110311]

Konttinen YT, Tensing E, Laine M, Porola P, Törnwall J, Hukkanen M. Abnormal distribution of aquaporin-5 in salivary glands in the NOD mouse model for Sjögren's syndrome. J Rheumatol. 2005:1071–1075. [PubMed: 15940770]

Larsen HS, Aure MH, Peters SB, Larsen M, Messelt EB, Kanli Galtung H. Localization of AQP5 during development of the mouse submandibular salivary gland. J Mol Histol. 2011; 42(1):71–81. [PubMed: 21203896]

Lavoie T, Lee B-H, Nguyen C. Current concepts: mouse models of Sjögren's syndrome. J Biomed Biotechnol. 2011; 2011:1–14.

Lodde BM, Mineshiba F, Kok MR, Wang J, Zheng C, Schmidt M, Cotrim AP, Kriete M, Tak PP, Baum BJ. NOD mouse model for Sjögren's syndrome: lack of longitudinal stability. Oral Dis. 2006; 12:566–572. [PubMed: 17054769]

Ma T, Song Y, Gillespie A, Carlson EJ, Epstein CJ, Verkman AS. Defective secretion of saliva in transgenic mice lacking aquaporin-5 water channels. J Biol Chem. 1999; 274:20071–20074. [PubMed: 10400615]

Makino S, Kunimoto K, Muraoka Y, Mizushima Y, Katagiri K, Tochino Y. Breeding of a non-obese, diabetic strain of mice. Exp Anim. 1980; 29:1–13.

Mavragani CP, Moutsopoulos HM. The geoepidemiology of Sjögren's syndrome. Autoimmun Rev. 2010; 9:A305–A310. [PubMed: 19903539]

Mellas RE, Leigh NJ, Nelson JW, McCall AD, Baker OJ. Zonula occludens-1, occludin and E-cadherin expression and organization in salivary glands with Sjögren's syndrome. J Histochem Cytochem. 2014; 63:1–12.

Molina C, Alliende C, Aguilera S, Kwon Y-J, Leyton L, Martínez B, Leyton C, Martinez B, Pérez P, González M-J. Basal lamina disorganisation of the acini and ducts of labial salivary glands from patients with Sjögren's syndrome: association with mononuclear cell infiltration. Ann Rheum Dis. 2006; 65:178–183. [PubMed: 16014676]

Nashida T, Yoshie S, Haga-Tsujimura M, Imai A, Shimomura H. Atrophy of myoepithelial cells in parotid glands of diabetic mice; detection using skeletal muscle actin, a novel marker. FEBS Open Biol. 2013; 3:130–134.

Nelson DA, Manhardt C, Kamath V, Sui Y, Santamaria-Pang A, Can A, Bello M, Corwin A, Dinn SR, Lazare M, Gervais EM, Sequeira SJ, Peters SB, Ginty F, Gerdes MJ, Larsen M. Quantitative single cell analysis of cell population dynamics during submandibular salivary gland development and differentiation. Biol Open. 2013; 2:439–447. [PubMed: 23789091]

Palmer RM, Eveson JW, Gusterson BA. "Epimyoepithelial" islands in lymphoepithelial lesions: an immunocytochemical study. Virchows Arch Pathol A. 1986; 408:603–609.

Perez-Moreno M, Jamora C, Fuchs E. Sticky business: orchestrating cellular signals at adherens junctions. Cell. 2003; 112:535–548. [PubMed: 12600316]

Redman RS. Myoepithelium of salivary glands. Microsc Res Technol. 1994; 27:25–45.

Redman RS. On approaches to the functional restoration of salivary glands damaged by radiation therapy for head and neck cancer, with a review of related aspects of salivary gland morphology and development. Biotech Histochem. 2008; 83:103–130. [PubMed: 18828044]

Rios AC, Fu NY, Lindeman GJ, Visvader JE. In situ identification of bipotent stem cells in the mammary gland. Nature. 2014; 506:322–327. [PubMed: 24463516]

Schindelin J, Arganda-Carreras I, Frise E, Kaynig V, Longair M, Pietzsch T, Preibisch S, Rueden C, Saalfeld S, Schmid B, Tinevez J-Y, White DJ, Hartenstein V, Eliceiri K, Tomancak P, Cardona A. Fiji: an open-source platform for biological-image analysis. Nat Methods. 2012; 9:676–682. [PubMed: 22743772]

Shiboski S, Shiboski C, Criswell L, Baer A, Challacombe S, Lanfranchi H, Schiødt M, Umehara H, Vivino F, Zhao Y, Dong Y, Greenspan D, Heidenreich A, Helin P, Kirkham B, Kitagawa K, Larkin G, Li M, Lietman T, Lindegaard J, McNamara N, Sack K, Shirlaw P, Sugai S, Vollenweider C, Whitcher J, Wu A, Zhang S, Zhang W, Greenspan J, Daniels T. American college of rheumatology classification criteria for Sjögren's syndrome: a data-driven, expert consensus approach in the SICCA cohort. Arthritis Care Res. 2012; 64:475–487.

Author Manuscript Author Manuscript Author Manuscript Author Manuscript

Soyfoo MS, De Vriese C, Debaix H, Martin-Martinez MD, Mathieu C, Devuyst O, Steinfeld SD, Delporte C. Modified aquaporin 5 expression and distribution in submandibular glands from NOD mice displaying autoimmune exocrinopathy. Arthritis Rheum. 2007; 56:2566–2574. [PubMed: 17665453]

Steinfeld S, Cogan E, King LS, Agre P, Kiss R. Abnormal distribution of aquaporin-5 water channel protein in salivary glands from Sjögren's syndrome patients. Lab Investig. 2001; 81:143–148. [PubMed: 11232635]

Tamgadge S, Tamgadge A, Satheesan E, Modak N. Myoepithelial cell – a morphologic diversity – a review. Res Rev A J Dent. 2013; 4:5–13.

Tincani A, Andreoli L, Cavazzana I, Doria A, Favero M, Fenini M, Franceschini F, Lojacono A, Nascimbeni G, Santoro A, Semeraro F, Toniati P, Shoenfeld Y. Novel aspects of Sjögren's syndrome in 2012. BMC Med. 2013; 11:1–17. [PubMed: 23281898]

Tucker AS. Salivary gland development. Semin Cell Dev Biol. 2007; 18:237–244. [PubMed: 17336109]

Tzioufas AG, Kapsogeorgou EK, Moutsopoulos HM. Pathogenesis of Sjögren's syndrome: what we know and what we should learn. J Autoimmun. 2012; 39:4–8. [PubMed: 22326205]

Vitale-Cross L, Amornphimoltham P, Fisher G, Molinolo AA, Gutkind JS. Conditional expression of K- ras in an epithelial compartment that includes the stem cells is sufficient to promote squamous cell carcinogenesis. Cancer Res. 2004; 64:8804–8807. [PubMed: 15604235]

Vitali C, Bombardieri S, Jonsson R, Moutsopoulos HM, Alexander EL, Carsons SE, Daniels TE, Fox PC, Fox RI, Kassan SS, Pillemer SR, Talal N, Weisman MH. Classification criteria for Sjögren's syndrome: a revised version of the European criteria proposed by the American-European Consensus Group. Ann Rheum Dis. 2002; 61:554–558. [PubMed: 12006334]

Wang D, Iwata F, Muraguchi M, Ooga K, Ohmoto Y, Takai M, Mori T, Ishikawa Y. Correlation between salivary secretion and salivary AQP5 levels in health and disease. J Med Invest. 2009; 56(Suppl):350–353. [PubMed: 20224222]

Xuan J, Shen L, Malyavantham K, Pankewycz O Jr, Ambrus JLA, Suresh JL. Temporal histological changes in lacrimal and major salivary glands in mouse models of Sjögren's syndrome. BMC Oral Health. 2013; 13:51. [PubMed: 24093879]

Zuo W, Zhang T, Wu DZ, Guan SP, Liew A-A, Yamamoto Y, Wang X, Lim SJ, Vincent M, Lessard M, Crum CP, Xian W, McKeon F. Lung regeneration mechanism discovered. Sci Dly. 2014; 517:616–620.
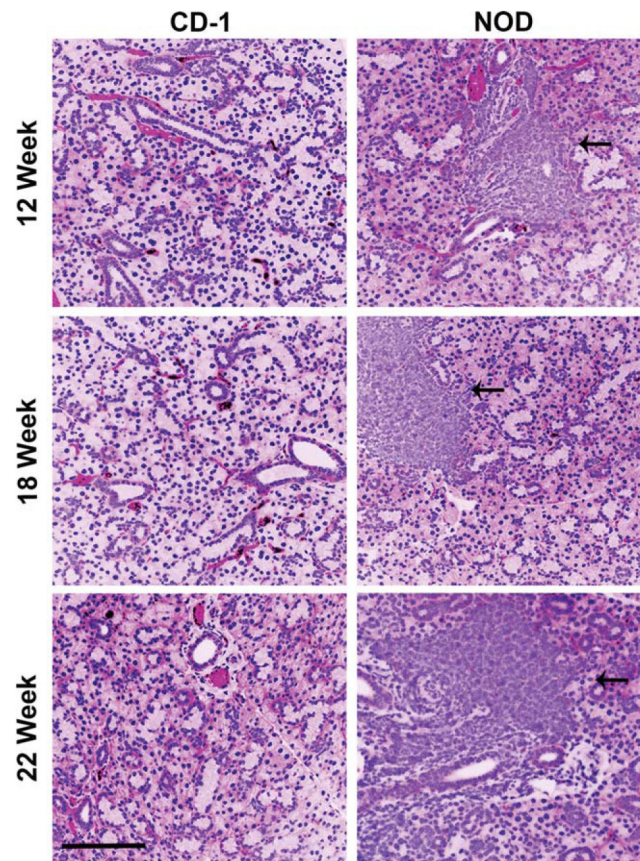
Fig. 1.
NOD/ShiLtJ and CD-1 mouse submandibular salivary gland (SMG) morphology. Mouse SMG virtual H&E stains for representative tissue samples from 12, 18, and 22 week old CD-1 (healthy control) and NOD/ShiLtJ female mice demonstrating increasing focal infiltrates with disease progression (indicated by black arrows). 12-week CD-1 n =6, 12 week-NOD n =6, 18-week CD-1 n =6, 18-week NOD n =5, 22-week CD-1 n =5, 22-week NOD n =5. Scale bar, 100 μm.
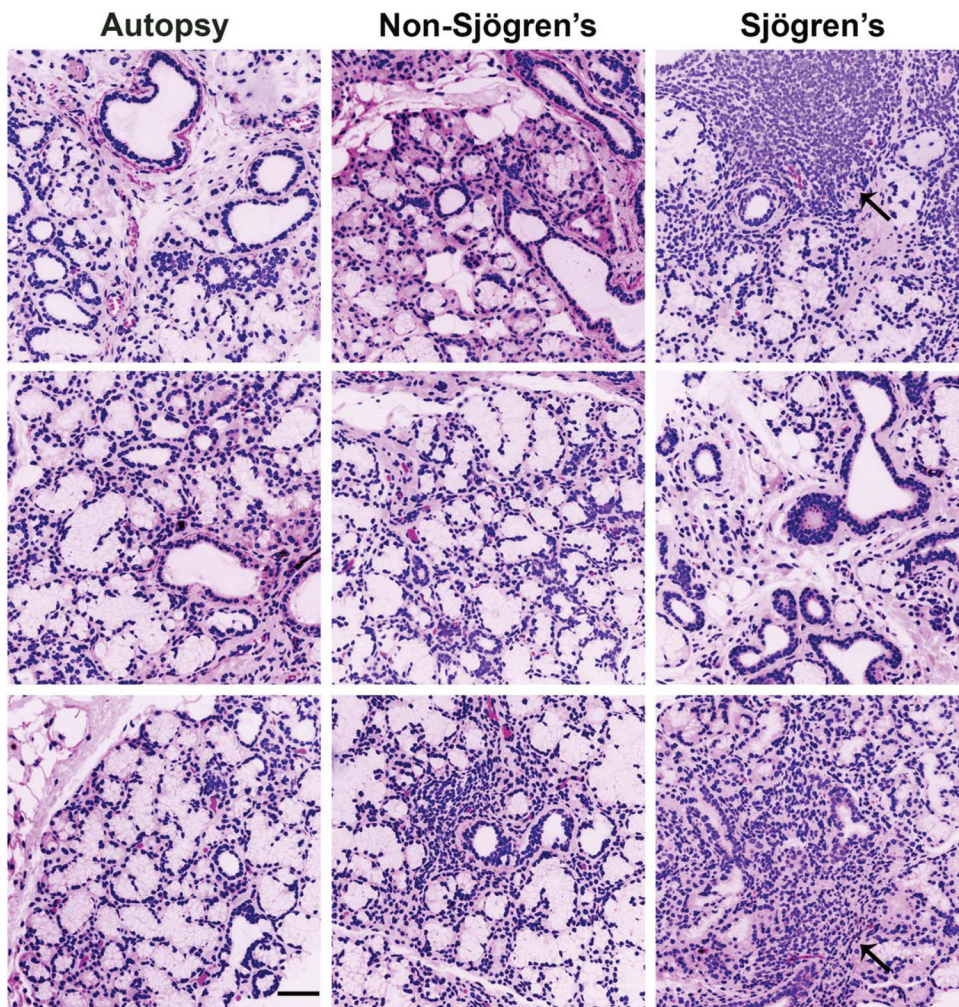
Fig. 2.
Human SS, non-SS, and autopsy labial salivary gland morphology. Human labial salivary gland virtual H&E stains for three representative samples from autopsy (control), non-SS patients (not diagnosed with SS due to lack of presence of autoantibodies and focus scores below 1), and diagnosed SS patients, demonstrating increased focal infiltrates in SS diagnosed patients (indicated by black arrows). SS, n =8, (average age 60, all female patients); non-SS, n =6 (average age of 52, all female patients); and autopsy, n =7 (average age 65, five male and two female patients). Scale bar, 100 μm.
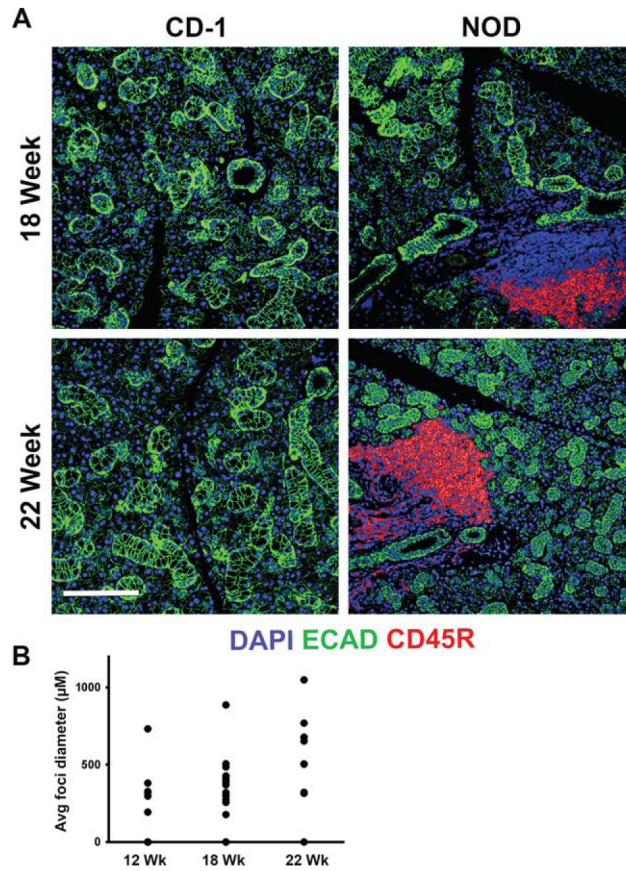
Fig. 3.

Lymphocytic infiltrates in NOD/ShiLtJ SMG. (**A**) Nuclear accumulations were identified as lymphocytic infiltrations using an antibody targeting CD45R (red) in the NOD/ShiLtJ mouse SMG. Areas of infiltrate are positive with DAPI staining (blue) but are not positive for the epithelial marker, E-cadherin (ECAD) (green). Scale bar, 100 μm. (**B**) Lymphocytic infiltrations were measured at their widest point. Progressive increases in largest lymphocytic infiltration size are apparent between 12, 18, and 22 weeks in the NOD/ShiLtJ tissues; no infiltrations were detected in CD-1 tissues at any age.
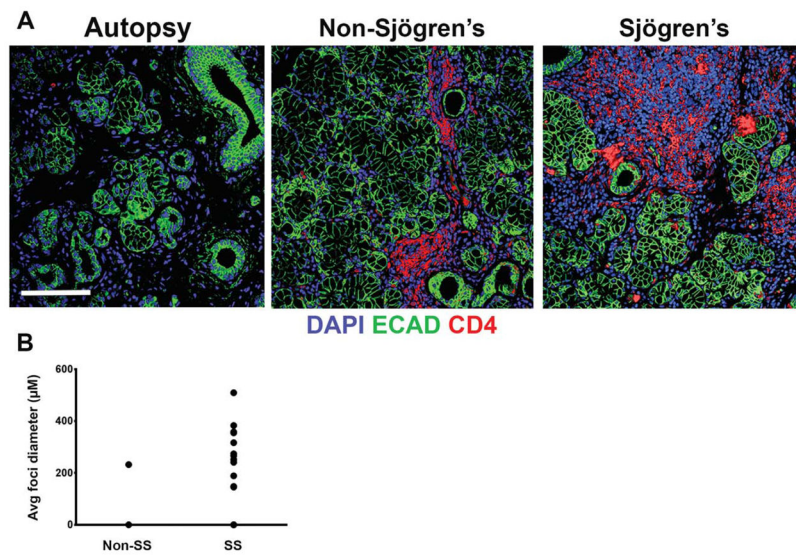
Fig. 4.
Lymphocytic infiltrates in human labial salivary glands. (**A**) Lymphocytic infiltrations were identified using an antibody targeting CD4 (red) in the human SS tissues. Areas of infiltrate are positive with DAPI staining (blue) but are not positive for the epithelial marker, ECAD (green). Scale bar, 100 μm. (**B**) Lymphocytic infiltrates were measured at their widest point. Measurements of infiltrates in human SS samples had a wide range of sizes, while few non-SS tissues contained infiltrates; No infiltrates were found in any autopsy tissues.
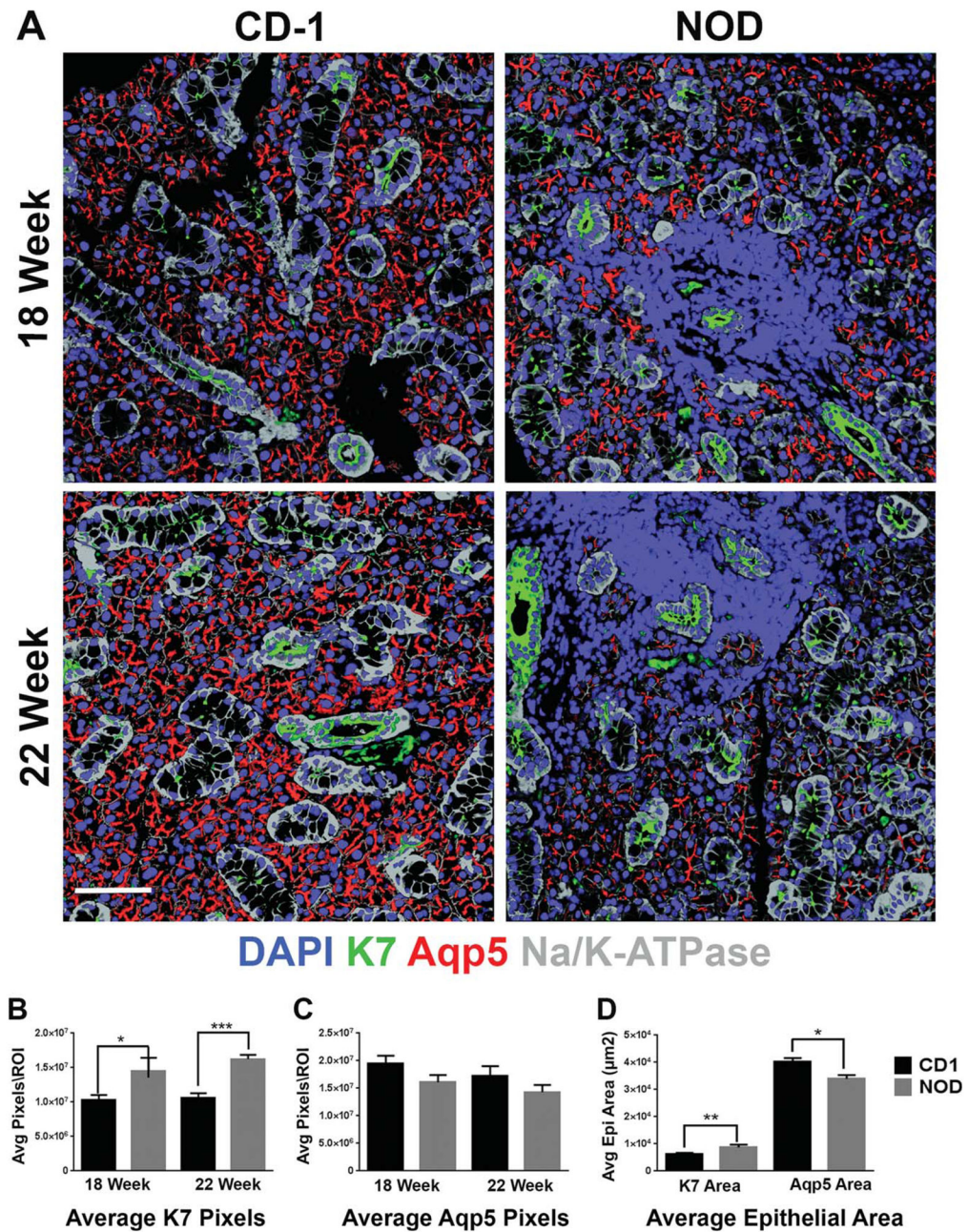
Fig. 5.
Significant increase in K7-positive ductal population in the NOD/ShiLtJ SMG. (**A**) NOD/
ShiLtJ and CD-1 mouse SMG tissue sections were subjected to IF for the ductal marker, K7
(green), acinar marker aquaporin 5 (Aqp5) (red), and epithelial marker Na/K-ATPase (gray)
together with DAPI staining (blue) for nuclei. A significant increase in K7, and slight
decrease in Aqp5 correlating with disease progression was observed in the NOD/ShiLtJ
mouse samples as compared with the CD-1 control tissues. Scale bar, 100 μm. (**B**) The
number of pixels was measured within regions of interest (ROI) for K7 and (**C**) Aqp5. (**D**)
The epithelial area (μm^2) covered by K7 or Aqp5 staining was measured in 22-week samples

and a significant increase was seen in the percentage of the epithelial area covered by ductal cells as compared with acinar cells. *P 0.05, **P 0.01, and ***P 0.001. Samples compared included CD-1 18-week (n =6), NOD/ShiLtJ 18-week (n =5), CD-1 22-week (n =5), and NOD/ShiLtJ 22-week (n =5).
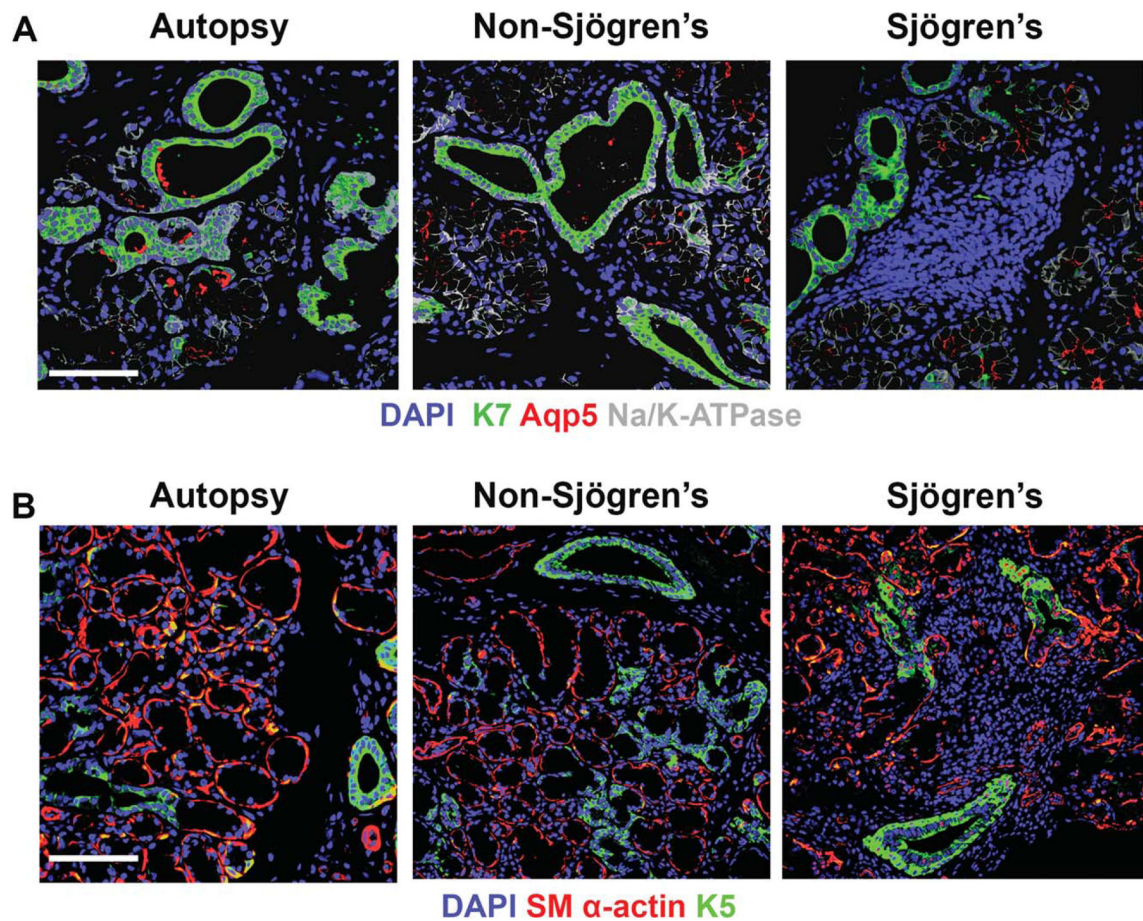
Fig. 6.
Immunofluorescence of human labial salivary glands for K7, Aqp5, K5, and SM α-actin. (**A**) Human labial salivary gland samples were stained for K7 (green) to mark the ductal population, which seems to increase in the SS samples, Aqp5 (red) to mark the acinar population, and Na/K-ATPase (gray) to mark the epithelial areas of the tissue along with DAPI (blue) to mark nuclei. (**B**) Human salivary gland samples were also subjected to staining for K5 (green) to mark the putative progenitor population and SM α-actin (red) to mark the myoepithelium along with DAPI (blue) to mark nuclei. Areas of the epithelium co-positive for K5 and SM α-actin (yellow) were found in autopsy tissues, and in some of the non-SS and SS tissues. SS, n =8, (average age 60, all female patients); non-SS, n =6 (average age of 52, all female patients); and autopsy, n =7 (average age 65, five males and two female patients). Scale bar, 100 μm.
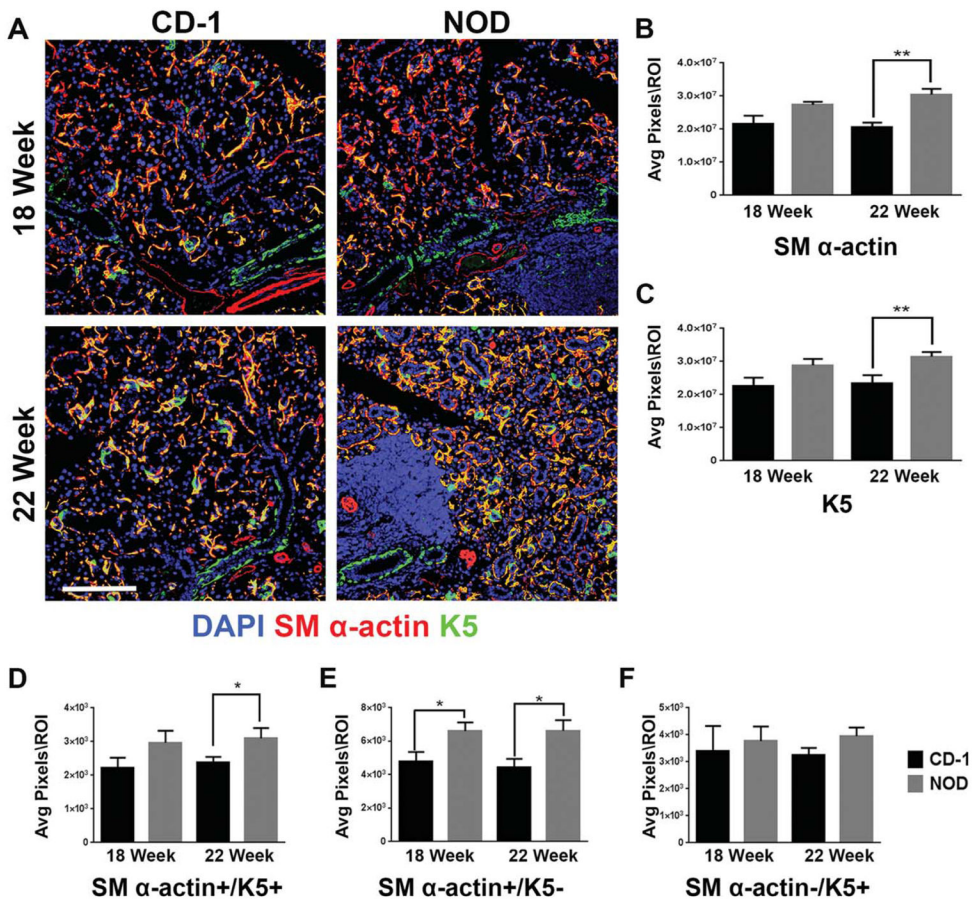
Fig. 7.
Identification of a SM α-actin/K5 co-positive cell population in the NOD/ShiLtJ SMG. (**A**) CD-1 and NOD/ShiLtJ SMG tissues were stained for K5 (green) and SM α-actin (red) and images were registered and merged with DAPI (blue). An increase in SM α-actin/K5 co-positive areas were detected in 18 and 22-week NOD/ShiLtJ SMGs (yellow). (**B–F**) Numbers of pixels were measured in regions of interest (ROI) within the epithelium of mouse NOD/ShiLtJ and CD-1 SMG for (B) SM α-actin, and (C) K5 and (D) SM α-actin/K5 co-positive (yellow). Total pixel levels for single positive cell populations were also quantified (E) SM α-actin$^+$/K5$^-$ and (F) SM α-actin$^-$/K5$^+$. CD-1 18- and 22-week n =5, NOD 18-week n =6, NOD 22-week n =5. *P 0.07, and **P 0.01. All scale bars, 100 μm.